Kinematic and rheological controls on rift-related fault evolution

Sophie Pan[1*], John Naliboff[2], Rebecca Bell[1] and Chris Jackson[3]

[1]Department of Earth Science and Engineering, Imperial College, Prince Consort Road, London, SW7 2BP, UK

[2]Department of Earth and Environmental Science, New Mexico Institute of Mining and Technology, NM, USA

[3]Department of Earth and Environmental Sciences, The University of Manchester, Williamson Building, Oxford Road, Manchester, M13 9PL, UK

[*]Corresponding author: Sophie Pan (sophie.pan@bp.com)

Key Points:

- Numerical models are qualitatively and quantitatively comparable to observational fault networks
- The scaling distribution of fault strain is not entirely power-law as there is a characteristic upper-bound limit
- Off-fault (i.e. non-extracted) deformation is significant in all models, accommodating from 25-45% of extension depending on rift parameters.

Abstract

Continental extension is primarily accommodated by the evolution of normal fault networks. Rifts are shaped by complex tectonic processes and it has historically been difficult to determine the key rift controls using only observations from natural rifts. Here, we use 3D thermo-mechanical, high-resolution (<650 m) forward models of continental extension to investigate how fault network patterns vary as a function of key rift parameters, including extension rate, the magnitude of strain weakening, and the distribution and magnitude of initial crustal damage. We quantitatively compare modelled fault networks with observations of fault patterns in natural rift, finding key similarities in their along-strike variability and scaling distributions. We show that fault-accommodated strain summed across the entire 160 x 160 km study area increases linearly with time. We find that large faults do not abide by power-law scaling as they are limited by an upper finite characteristic, ω_0. Fault weakening, and the spatial distribution of initial plastic strain blocks, exert a key control on fault characteristics. We show that off-fault (i.e. non-fault extracted) deformation accounts for 30-70% of the total extensional strain, depending on the rift parameters. As fault population statistics produce distinct characteristics for our investigated rift parameters, further numerical and observational data may enable the future reconstruction of key rifting parameters through observational data alone.

1 Introduction

Rifts are globally widespread, yet display a wide variety of structural styles (Fig. 1) as a result of crustal rheology (Buck, 1991; Ebinger et al., 1999), rift obliquity (Corti, 2008), the presence of pervasive lithological and mechanical heterogeneities (Fletcher and Hallet, 1983; Morley 1999), extensional velocity (Buck, 1991; Huismans and Beaumont, 2003), thermo-isostasy and loading (Kooi et al., 1992), crustal melting and magmatism (Rey et al., 2009; Corti et al., 2003), and syn-extension erosion and sedimentation (Burov 1997). While there is a global understanding of what parameters influence rift evolution and the final structure of rifted margins, the interaction and feedback of such intrinsically complex processes is still poorly constrained (Peron-Pinvidic et al., 2019). As rifts are characterised by the structural development of normal fault populations, the underlying rift controls may potentially be coded into the kinematics and geometry of rift-related normal fault networks.

Normal faults produce extensive networks of discontinuities at the surface and subsurface, at length scales ranging from millimetres to hundreds of kilometres (e.g. Willimese 1996; Schultz and Fossen, 2008). With increasing brittle strain, faults nucleate within the crust and lengthen and gain displacement to eventually form a through-going fault system (Cowie et al., 2000). Fault systems enable the trapping of carbon dioxide (Kaldi et al., 2013) and hydrocarbons (Sorkhabi and Tsuji, 2005). The discontinuities within complex normal fault populations are particularly favourable for geothermal energy production (Faulds et al., 2015; Coolbaugh et al., 2006). Our understanding of how fault populations are characterised and how they evolve through time is thus crucial to the identification of potential energy storage and waste sites.

Faults have been recognised to exhibit scaling properties that describe the size distributions of fault length, displacement and the spatial distribution of the fault network (Cowie et al., 1995, Fig. 2). These properties provide insights into the underlying physical mechanism of fault nucleation and growth (Cowie 1998). Field-data of faults commonly observe a power-law distribution, i.e. they are scale invariant (Kakimi 1980; Scholz and Cowie, 1990; Walsh et al., 1991; Jackson and Sanderson, 1992; Marrett and Allmendinger, 1992; Villemin et al., 1995), similar to the Gutenberg-Richter relationship observed for earthquakes (Gutenberg and Richter, 1956; Kanamori and Anderson, 1975). However, numerical (Ackermann et al., 2001), physical (Spyropoulos et al., 1999) and observational (Cowie et al., 1993; Gupta and Scholz, 2000; Soliva and Schultz, 2008) studies of fault length distributions suggest that faults may scale exponentially in higher strain settings (Fig. 2). This has implications for the forecasting of the size, and density of sub-resolution faults, which typically uses a power-law distribution for extrapolation (e.g. Marrett and Allmendinger, 1991; Torabi et al., 2011). Sub-seismic faulting has a profound effect on (CO_2 or hydrocarbon) reservoir performance, as it may enhance or reduce reservoir permeability and overall flow properties (e.g. Antonellini and Aydin, 1994; Damsleth et al., 1998; Ferrill et al., 2009).

It has been difficult to deduce the true scaling nature of fault networks, as data are usually obtained from mapping which contains an insufficient range of fault numbers (Cladouhos and Marrett, 1996; Scholz 1997). Often fault observations span only 1 order of magnitude in terms of fault scale (Bonnet et al., 2001) and the limited spatial extent incurs sampling biases (Pickering et al., 1995). The finite size of datasets leads to underestimation of small faults due to limited resolution (truncation) and undersampling of the largest faults (censoring), which overall alter the appearance of the distribution (Fig. 2) and may lead to erroneous conclusions of the style and factors controlling fault patterns. Previous statistical strain analyses are often presented in 1D (through borehole images and well logs) or 2D (fault lengths in outcrop or summing heaves across cross sectional transects; Walsh et al., 1991; Marrett and Allmendinger, 1991; Cowie et al., 1995; Gupta and Scholz, 2000; Torabi et al., 2011). It remains a challenge to extrapolate results obtained from 1D and 2D datasets to 3D systems (Bonnet et al., 2001).

In addition to the lack of spatially extensive datasets in active and ancient rifts, there are even fewer temporally constrained datasets. Earthquakes only provide a short snapshot in time relative to the long geological timescales in which they accumulate. Few faults are associated with age-constrained growth strata that record fault activity over geological timescales (e.g. Meyer et al., 2002). The lack of kinematic constraint has led to different models of how individual faults grow (e.g. Walsh et al., 2002; Rotevatn et al., 2019; Pan et al., 2022a). Furthermore, it is unclear how other forms of deformation (i.e. diffuse, ductile or aseismic slip) are accommodated during extension. Limitations in spatial and temporal resolution from observational data means there is little understanding of how fault networks evolve quantitatively, and even less understanding of how underlying rift dynamics may govern the geometry and kinematics of natural rift fault networks.

Here, we utilise high resolution (<650 m), 3D thermo-mechanical forward models of lithospheric deformation to investigate the effect of well known, first-order rift controls, such as extension rate and rheology, on the structural expression of normal fault network evolution. The along-strike variability revealed by the 3D models enable key fault attributes, such as the length, active and cumulative strain, and strike, to be extracted across a range of spatial scales throughout their evolution. We characterise the scaling distribution of fault accommodated strain through time, and investigate how different model parameters affect the overall geometry of the fault network in 3D. We compare differences between measured crustal strain in the models with the summation of strain accommodated by normal faults, resulting in off-deformation percentage estimates for each model. Finally, we compare the modelled fault statistics with those observable in the Earth's crust, allowing us to better understand and potentially infer first-order controls on rift dynamics, based on observed fault patterns.

2 Methods

2.1. Model description and setup

The open-source dynamics code ASPECT (Kronbichler et al., 2012; Heister et al., 2017) is used to model 3D continental extension. The thermomechanical model solves the incompressible Boussinesq approximation of momentum, mass and energy equations, combined with advection-diffusion equations. For a full description of the governing equations, see Naliboff et al. (2020) and Pan et al. (2022b). The governing equations are solved on a 3D gridded domain spanning 500 x 500 x 100 km (X, Y and Z respectively). The grids are 5 km resolution at the sides and base of the model, and we use an adaptive mesh refinement to successively reduce this down to 625 m over a 180 x 180 x 20 km region in the centre of the model. Velocities are prescribed to the left and right of the model. Inflow at the model base balances the outflow, and the top of the model is a free surface (Rose et al., 2017).

The model contains three compositional layers: the upper crust (0-20 km), the lower crust (20-40 km), and the mantle lithosphere (40-100 km). Viscous flow laws for dislocation creep are wet quartzite (Gleason and Tullis, 1995), wet anorthite (Rybacki et al., 2006) and dry olivine (Hirth and Kohlstedt, 2003) containing background densities of 2700, 2800 and 3300 kg m^{-3}. The temperature distribution follows a characteristic conductive geotherm for the continental lithosphere (Chapman, 1986) where the temperature at the base of each layer is 633, 893 and 1613 K (for parameters and assumptions used to solve for the conductive profile, see Supplementary Table 1).

The compositional layers deform through a combination of nonlinear viscous flow (following dislocation creep) and brittle plastic deformation (Glerum et al., 2018). Brittle deformation follows a Drucker Prager yield criterion:

$$\sigma'_{II} = \frac{6C\cos\phi \; + \; 2P\sin\phi}{\sqrt{(3 + \sin\phi)}}$$

Where the initial friction angle (ϕ) and cohesion (C) are 30 and 20 MPa, and they linearly weaken as a function of finite plastic strain (see Fig. 3). Following Duretz et al. (2020) the Drucker Prager yield criterion is modified further to include a plastic (viscous) damper, which acts as a stabilization term for the shear band width and produces mesh-independent results provides a sufficient resolution to resolve the damper viscosity (1e21 Pa s here).

Instead of a single zone of initial weakness, a distribution consisting of binary strong and weak blocks of plastic strain are prescribed in the upper crust, following Pan et al. (2022b). The statistically randomised method geologically mimics variations in the initial strain field that may reflect the mechanical properties of the rifting plate (e.g. Scholz and Contreras, 1998), the presence of the pervasive and/or discrete fabrics (e.g. Versfelt and Rosendahl, 1989) and stronger regions such as cratons (e.g. Dunbar and Sawyer, 1989; Versfelt and Rosendahl, 1989; Tommasi and Vauchez, 2001; Ziegler and Cloetingh, 2004; Buiter and Torsvik, 2014). Overall the initial strain field promotes the development of a complex fault network displaying the along-strike variability in strike and displacement observed in natural rifts.

In this paper, the plastic strain in the reference model (Model A) consists of strong and weak values of 0.5 and 1.5 spatially over 2.5 km^2 blocks, with the friction angle and cohesion weakening by a factor of 2 over the plastic strain interval. Relative to the reference model, we investigate the effect of an increased spatial wavelength of 5 km blocks (Model E; Fig 3), weakening the friction angle and cohesion by a factor of 4 (Model D) and reducing the contrast between blocks to 0.5 and 0.6 (i.e. faster brittle weakening; Model C). We also investigate extension rates of 1.25 and 5 mm/yr (see Fig. 3); these correspond to a range comparable to those characterising slow active rifts (e.g. East Africa, Basin and Range) using GPS data (e.g. Argus and Helflin 1995).

2.2. Fault network extraction

Fault analysis is sampled on a horizontal plane located 5 km beneath the initial model surface as the full extent of the fault network is captured at this level (Fig. 5). Fault statistics are extracted using an image-processing workflow from Pan et al. (2022b), which derives the strain profile gradient from the active deformation field. This approach effectively defines a fault as a region of clearly localised active slip, and enables the extraction of discrete fault segments within a complex, interacting fault network (Fig 5c). Each fault label contains a unique accessible index, and each label acts as a mask in order to extract active and finite strain, as well as to compute geometries such as fault length and strike. In Pan et al. (2022b), fault labels are thinned so that they are 1 element width along the fault in order to derive the cumulative euclidean distance (i.e. fault length). In contrast, here the thinned labels are later enlarged (morphologically dilated using a structuring element - see Supplementary Material for full details), in order to capture the full extent of shear zone deformation, which typically span 2-3 grid elements (Fig. 5c-d). The total strain occupied and extracted by each fault label is therefore equivalent to the geometric moment, M_g (see next section 2.3).

2.3. Fault strain summation

Incremental strain is often calculated in earthquake seismology using the Kostrov summation method (Kostrov 1974, Molnar 1983). Similarly, strain on faults over geological timescales can be determined using the geometric moment, M_g:

$$M_g = u_{ave} n$$

where u_{ave} is the average displacement and n is the fault surface area. The geometric moment is directly related to the seismic moment (which is the geometric moment divided by the shear modulus; Scholz 1989) allowing for comparison of faults active over geological timescales with the Gutenberg-Richter power-law population of characteristic earthquake populations (Gutenberg and Richter, 1944; Kanamari and Anderson 1975; Scholz and Cowie 1990). Summation of the geometric moment divided by the area of regional interest (V) allows for an estimation of strain, ε (Marrett and Allmendinger 1990; Molnar 1983):

$$\varepsilon = \sum_{k=1}^{n} \frac{M_g^k}{V}$$

The above equation results in the total strain accommodated by the fault network (i.e. Fig. 5e). In addition to the strain occupied by our extracted faults (i.e. Fig. 5d), we also sum the total crustal strain, ε (i.e. Fig. 5a) and active strain (i.e. Fig. 5b) over the central 180 x 180 km high-resolution zone. As a result, the difference between the total crustal strain and fault strain equates to off-fault deformation (see Supplementary Figure 2).

2.4. Fault scaling distributions

The equation of a power law fault population distribution (e.g. Kakimi, 1980; Villemin and Sunwoo, 1987; Childs et al., 1990; Scholz and Cowie, 1990; Walsh et al., 1991) follows:

$$N(> \omega) = A\ \omega^{-\alpha}$$

where ω is the measure of size (e.g. length, displacement or geometric moment), N is the cumulative number of values ≥ ω, A is a constant and α is the exponent. A log transformation of this equation gives a linear relationship between log N and log ω, with the slope gradient representing the power law component, α (Fig. 2).

An exponential scaling distribution better describes fault length distributions (Cowie et al., 1993; Ackermann et al., 2001; Spyropoulos et al,. 2002) and follows:

$$N(> \omega) = A \exp\left(\frac{-\omega}{\omega_0}\right)$$

where the exponential law incorporates a characteristic scale ω_0, which may reflect a physical length in the system such as layer thickness (Cowie, 1998).

The gamma distribution is more commonly used in earthquake statistics (Davy 1993) but it also characterises fault trace lengths in the Gulf of Corinth rift (Michas et al., 2015). The gamma law follows:

$$N(> \omega) = A\omega^{-\alpha} exp_q \left(\frac{-\omega}{\omega_0}\right)$$

The gamma law distribution combines a power law from equation 4 with an exponential tail from equation 5 (Fig. 2).

We used curve fitting and applied a non-linear least squares fit to find the optimal set of parameters for the defined function (equations 4-6). We use the geometric moment (see Section 2.3) in order to analyse the scaling distribution of strain, where the initial input variables for A, α, q and ω_0 are the fault number, 1, 0, and the mean fault strain, respectively (following a similar methodology from Cowie et al,. 2012). Only the best fitted distribution is shown in figures for clarity, however the parameters for other distributions are shown in the Supplementary Fig. 1. We assume that the smallest 30 faults are affected by truncation as the data points characteristically flatten off at this point in all models. The smallest 30 faults are therefore discarded for curve fitting, and the remaining number of faults is sufficiently large across several orders of magnitude (between 200-500 faults depending on the model) to provide a robust statistical analysis. We further discuss the implications of sampling bias in the discussion.

3 Results

3.1. Modelled fault network evolution

The general behaviour of the modelled fault network and their corresponding statistics are first described using reference Model A. All models show that fault network template is established from the initial onset of extension (Supplementary Video 1). In the first resolvable time increment (at 0.1 Myrs), the reference model A consists of a diffuse network of deformation across the model domain (Supplementary Video 1). From 0.1 - 0.5 Myrs, active deformation shows a reduction in element width as shear zones actively localise on the fault template - we attribute this behaviour as the full establishment of fault pattern lengths. After 1 Myrs of extension, a number of fault maximas appear randomly distributed throughout the model, and strain predominantly accumulates on the initial maxima points (Supplementary Video 1). The evolution of all models demonstrate similar general behaviour of widespread strain localisation, from an initially distributed deformation field, to a localised, large normal fault array (e.g. Cowie et al., 2000; Gawthorpe et al., 2003). While all investigated models reveal that fault patterns are established early and strain localises with extension, the fault pattern template and style of subsequent strain deformation exhibit considerable variability across the investigated rift parameters (Fig. 4).

The cumulative frequency of fault strain of reference model A shows a curved distribution similar to many other natural observations of fault scaling (e.g. Meyer et al., 2002; Soliva and Schultz, 2008). Power-law, exponential scaling, and gamma distributions all fit the observational data to $R^2 \geq 0.99$, although the high R^2 value is attributed to the logarithmic nature of the dataset. We find that the gamma has the highest R^2, and critically, best matches the largest faults in the model (Supplementary Figure 1; Fig. 6a). Fig. 6a shows that up to 0.5 Myrs extension, the total number of faults increases as the strain increases - we correlate this to an ‘initiation’ phase where deformation quickly localises and the lengths of the fault network pattern are fully established. For the remainder of extension, the fault distribution profile moves towards the right as faults increasingly accommodate strain, and the total number of faults stays relatively constant (Fig. 6a). The parameters of best fit show that ω_0 increases with extension, and q ranges between 1-3. α stays relatively constant throughout time, ranging between 0.1-0.3 (Fig. 6a, Supplementary Video 2).

While the central portion of the fault distribution progressively accommodates strain, reflected by stable increases in α, faults accommodating the highest strain are variable throughout extension, where the magnitude of highest strain periodically fluctuates from the q-gamma fit trendline (Fig. 6a; Supplementary Video 2). We note that the periodic fluctuations of the fault distribution are sometimes initially marked by a break in slope on the log plots (e.g. see 1 and 3 Myrs distribution on Fig. 6a) resulting in the appearance of a prominent tail. The fluctuations above (i.e. strain greater than) the trendline correspond to continuous active slip events, where the summed strain along large fault lengths is high. Conversely, deviations below the trendline suggest that the strain intermittently accommodated by faulting is relatively distributed throughout the crust (rather than accommodated by a few large faults). The total summed strain accumulation, accommodated by the extracted fault network, increases approximately linearly through time, however there are small temporal fluctuations which reflect the oscillations between distributed and localised deformation (Fig. 6b).

3.2. Investigated rift model parameters

3.2.1. Extension rate

Models deforming at constant rates of 1.25 and 5 mm/yr (Models A and B; Fig. 3) allow for the investigation of extension rate on fault network evolution. The models show that higher extension rates (5 mm/yr) correspond to an overall higher magnitude of plastic strain deformation over increasingly diffuse regions (Fig. 7a and b). Our results also show that an increase in extension rates do not affect the overall spatial pattern of finite strain (Fig. 7a and b). For example, fault maximas and localisation occur on the same fault systems no matter the extension rate, although to some extent the fault strain magnitudes and shear width of deformation are variable across the investigated models (Fig. 7a and b).

Similar to the other investigated parameters, fault strain distributions for all models investigating extension rates abide by a q-gamma distribution (R2 > 0.99; Fig. 7). The distribution appears broadly similar across the investigated models, whereby greater extension rates accommodate higher strain throughout extension, so plot further towards the right in Fig. 7. For both models, ω_0 increases with extension, but overall magnitudes are higher for the 5 mm/yr model - at the final 5 Myrs timestep shown, ω_0 is 2.7x 10^6, 3 times higher than that of the 1.25 mm/yr model at 8.7 x 10^5 (Fig. 7). For the 2.5 mm/yr model, alpha steepens from 0.21 to 0.07 from 1 to 2 Myrs, respectively, before increasing for the remainder of extension (Fig. 7a). For the 5 mm/yr model, alpha increases (i.e. the central portion of the slope shallows) with extension, and reaches a relatively higher value of 0.32 by 5 Myrs extension (in contrast to 0.2 for the 1.25 mm/yr model).

3.2.3. Rheology

Our results indicate that changes to crustal rheology exert the most significant control on fault patterns, both visually due to along-strike variations in strike, strain, length and density, and statistically due to differences in their scaling distributions (Fig. 9). Most notably, models with relatively weak faults (Models C and D) contain less faults, thus strain is localised onto fewer, larger structures (Fig. 8b and d). The cumulative strain profiles of these two weak models reflect their localised behaviour, where the gradient of strain distribution trends shallower relative to the reference model (Fig. 9). The q-gamma fitted parameters show that highly localised fault populations such as Models C and D both exhibit lower α values of c. 0.03 and 0.09 and thus shallower trends for the central portion, and contain higher values of ω_0. Although the cumulative strain distributions are comparable between the two weak models (Model C and Model D), their fault template are significantly different whereby Model D exhibits significantly more pronounced along-strike variability (Fig. 8d).

Investigations into the spatial wavelengths within the initial distributions of plastic strain (Model A: 2.5 km^2 or Model E: 5 km^2) here reveal that strain scaling distributions appear comparable as both exhibit relatively higher α values (0.27 and 0.2, respectively) and lower ω_0 values (Fig. 8a and e). However, the faults in Model E overall accommodate less strain magnitude in their scaling distribution (Fig. 8e), and the visual style of the pattern of deformation differs significantly between the two models, with larger initial blocks producing more continuous, sinuous fault patterns with less along-strike variation (Fig. 8c).

3.3. Fault-accommodated strain through time

Fig. 9 shows the total fault accommodated strain through time across all models, and a snapshot of their fault strain distribution at 5 Myrs. For the cumulative distributions in Fig. 9a, the geometric moment observed from the NW Shelf of Australia (Meyer et al., 2002; Pan et al., 2022a) are shown. Fault strain from Pan et al. (2022a) is summed and divided by the studied area size (1200 km^2) for a dimensionless comparison of strain. Similarly from Bell et al. (2011), 2D cross-sectional strain across three transects across the Corinth Rift are divided by the rift width. Due to a range of uncertainty on the strain summation and age of rifting, we plot upper and lower bound estimates (see Supplementary Material for values).

Overall the 5 rift models reveal that summed fault strain increases linearly through time (Fig. 9b) when at constant extension rates. The rate at which summed fault strain increases is variable, and lower rates correlate to lower rates of extension (Fig. 9b). Within models of the same 5 mm/yr extension rate (Models A, C, D, E), higher rates of strain accumulation occur in models characterised by relatively weak crust and/or faults (i.e. Models C and D). Overall we find that the range of fault strain accumulation lies within the observational fault data (Fig. 10b).

Fig. 9a reveals that the strain scaling distribution of faults all exhibit the typical curvature characterised by observational datasets. Fault populations are best fit by a q-gamma distribution but exhibit variable fitted parameters, particularly q and ω_0. The lower 1.25 mm/yr extension rate model plots closest to the left, consistent with findings that it exhibits lower strain magnitude in comparison to the other models (Fig. 9a). In contrast, Models C and D with weaker strain mechanisms plot furthest to the right and thus their faults accommodate the highest strain magnitudes. Noticeably, these models are characterised by lower, shallower power law values (c. 0.11-0.15) and higher ω_0 values of c. $6x10^6$ (Fig. 9a).

3.4. Off-fault deformation

The summed difference between extracted fault accommodated strain and total crustal strain (e.g. Fig. 6) may account for diffuse deformation, which we term as off-fault deformation (OFD). Supplementary Fig. 2b shows how the OFD of Model A changes through time. OFD% rapidly decreases within the first 0.8 Myrs, which we correlate to fault organisation and initiation (Supplementary Fig. 2b). For the remainder of time, OFD% *progressively* reduces, corresponding to progressive strain localisation onto faults (Supplementary Fig. 2b). A similar model behaviour to the reference model is depicted in Fig. 10, where the majority of the scatter and outliers in the plot is due to the initiation phase in the first 1 Myrs. An exception is the model (B) with a slow extension rate (1.25 mm/yr), which shows a reverse trend of fault localisation from the onset of extension (Fig. 10). On average, Fig. 10 shows that OFD% accounts for approximately 40% in the models, ranging from 25% to 45% depending on the investigated rift parameters. We find that the model (C) with an increased rate (10x) of fault weakening contains the lowest proportion (25%), followed by the model (D) with a large magnitude (4x) of fault weakening - given the weakened mechanisms this corresponds to the high occurrence of strain localisation observed (Section 3.2.3).

4 Discussion

4.1. Fault strain comparison between numerical models and natural observations

The extraction of fault geometry within an entire fault population has enabled us to demonstrate that modelled faults are *quantitatively* comparable to fault geometries observed in rifts (Fig. 9). Modelled fault populations exhibit a curved distribution similar to size distributions observations in the literature for length (e.g. Scholz et al., 1993; Yielding et al., 1996; Odling, 1997), displacement (Marrett and Allmendinger, 1992; Knott et al., 1996) and geometric moment (e.g. Meyer et al., 2002; Bailey et al., 2005; Fig. 9a). The total fault strain of the models also quantitatively plot within the range of strain derived for observational data (Fig. 9b). Models which experienced 1.25 mm/yr rates of extension lie closest to the observational range for the Exmouth Plateau - taken at face value, this predicts that ancient extension rates are relatively low based on its magnitude strain through time.

Although our results have demonstrated that fault strain is largely comparable between models and observations, we find that direct rift inversions to recover rift parameters using summed strain measurements (i.e. Fig. 9b) are still not achievable due to uncertainties in i) measured observational strain, which is subject to interpretative biases and limited spatial resolution (e.g. Bonnet et al., 2001); and ii) overall rift duration, as the structure of active and ancient rifts observed provide only a snapshot in time, and there is often uncertainty on the age of the oldest syn-rift sediments to date the rift age as these deep sediments are rarely drilled. Fault backstripping may enable further data points of strain-time, however the earliest resolvable growth strata preserved in ancient systems rarely precedes 5 Myrs of rifting, therefore additional modelling of longer timescales may be needed for comparison.

4.2. Normal fault growth and rift evolution

The spatial and temporal scales covered by numerical modelling give insight on the earliest stages of fault growth, which are not easily constrained using seismic reflection and borehole data (Jackson et al., 2017). Here, all models establish their finite strain patterns from the nearly onset of extension, i.e. faults abide by the ‘constant-length’ model (Stage 1; Fig. 11) consistent with Walsh et al. (2002). The rapid establishment of fault patterns within the first <100 kyrs is attributed to the initial randomisation of the crustal (plastic) strain field. Our results demonstrate that the weaknesses in the initial plastic distribution control the loci for which strain maxima form (Stage 2; Fig. 11) and which eventually become the future sites of displacement accumulation (Stage 3; Fig. 11), similar to the findings of Cowie (1995). The behaviour of strain localisation onto through-going faults is consistent with Sornette et al. (1990), Cowie (1998) and Gupta et al. (1998), supporting that it is a fundamental characteristic of fault network evolution. While all models undergo strain localisation, models with larger (i.e. weaker) brittle strength contrasts between initial binary blocks or a faster rate of brittle weakening (C and D) trend more exponentially from the onset of extension (e.g. Fig. 8). The investigations of initial strain distribution in the models highlight the importance of crustal strength variations, which may be distributed randomly, or contain spatial significance i.e. pre-existing structures (e.g. Duffy et al., 2015), shear zones (e.g. Phillips et al., 2016) and terrane structures (e.g. Daly et al., 2014). We suggest that the relative and/or bulk strength from structural inheritances play an important role in structural development and may be further investigated through numerical modelling, where the initial strain field can be statistically quantified.

4.3. Fault strain scaling distribution evolution

Despite the assumption that faults abide by a power law scaling, we find that the distribution of the modelled faults is best described by a q-gamma distribution (a power law across moderate sized faults, with an exponential tail for the largest faults within a population), consistent with earthquake and seismic hazard assessments (Davy, 1993; Kagan 1997; Sornette and Sornette, 1999; Main 2000) and a study of a naturally occurring fault network in the Gulf of Corinth (Michas et al., 2015). Our results show that faults are not entirely fractal; instead, the distribution curve becomes steeper due to an upper bounding characteristic scale (e.g. Fig. 6). We argue that the large bound limit of the fault distribution in our results is real and is not due to censorship as the modelled area (180 x 180 km) is rift scale and is sufficiently large to capture the biggest strain-accommodating faults. Furthermore, the position at which the fall-off occurs is significantly greater than previous deductions of censorship effects, and occurs across all investigated models of different strain magnitudes. We speculate that the upper limit of fault distributions is related to similar upper bounding limits that define observational D-L profiles - faults cannot physically exhibit strain beyond a certain limit due to the thickness and strength of the crust (e.g. Cowie and Scholz, 1992).

Across all investigated model parameters, α remains relatively consistent between 0-0.3 and is comparable to similar scaling distributions of geometric moment from the NW Shelf of Australia (α = 0.4-0.5; Fig. 9). When fitted with a powerlaw distribution, the scaling exponent is c. 0.7 (consistent with existing literature which ranges between 0.3 - 2 (Villemin and Sunwoo 1987; Scholz and Cowie 1990; Turcotte et al., 2007; Marrett and Allmendinger 1992; Cladouhos and Marrett 1995; Yielding et al., 1996; Knott et al., 1996; Schlische et al., 1996). Previous numerical modelling (Cowie et al., 1993, 1994) and outcrop data (Wojtal 1986, 1994, 1996) suggest that the power-law scaling exponent decreases through time, due to the progressive concentration of strain onto large faults. While our models clearly exhibit progressive strain localisation, and the fault distributions here are visually comparable to those in aforementioned studies, our study correlates the behaviour of fault distribution profiles to the upper-bound exponential scaling characteristic, ω_0, which increases with time (Fig. 6, 9 and 11).

Our results demonstrate that while the majority of the fault network distribution steadily accumulates displacement through time (as the plot moves towards the right with consistent α), the tail-end of the distribution (i.e. strain accommodated on the largest faults) is more transient (Fig. 6). We correlate the transient behaviour of large faults to the complexity of the fault network and interaction of fault segments due to competing stress redistribution (e.g. Cartwright et al., 1995; Dawers and Anders, 1995). Here, the extracted faults exhibit long lengths when they interact, producing strike-continuous slip events, and subsequently strain is redistributed along the entire length of the fault system (across relay ramps) resulting in a high fault strain value. We find that the occurrence of a prominent tail in log plots (e.g. at 2 Myrs on Fig. 6; see also Fig. 11) may be reflective of linkage events for large faults, consistent with initial discussions from Wojtal et al. (1996). The break in slope on log-log plots and prominent tail is apparent in fault size distribution plots from experimental models (e.g. Ackermann et al., 2001), and field studies on Earth (e.g. Casey et al., 2003; Soliva and Schultz, 2008; Gudmundsson et al., 2013) and other planetary bodies (e.g. Vallianatos et al., 2016). While some studies discuss the presence of a prominent incipient tail (e.g. Walsh et al., 2003; Gudmundsson et al., 2013; Soliva and Schultz, 2008), its relevance is not fully characterised or understood, and we encourage future work to investigate its significance.

Our attempt to characterise scaling laws have highlighted how sampling protocols and fitting procedures can and have led to different outcomes (i.e. exponential, power law or a combination of both), particularly due to the effect of sampling biases. Specifically, the cut-off point used to account for truncation is highly subjective and often assumes a power law scaling distribution *a priori* (Supplementary Fig. 3). Historically, geoscientists perform a log-log transform of ω and $N(>\omega)$ (equation 4 in Methods; see Fig. 2 for log-log transform) and either fit by eye or use a least-squares estimation of the resulting straight line after truncating their data (Pickering et al., 1995). Such methods are not statistically validated and can produce inaccurate estimates (Clark et al., 1995; Bonnet et al., 2001; Clauset et al., 2009). We suggest that the inconsistency of such procedures have led to different scaling conclusions. For example, analogue modelling from Ackermann et al. (2002) found that size distributions changed from powerlaw to exponential. Similarly, observational data from Gupta and Scholz (2000) found that size distributions are power law for low strain, and exponential for high strain settings. In contrast, for fault distributions that appear similarly curved, Cowie (1995), Bonnet (1997) and Soliva and Schultz (2008) describe a transition from distributed to localised faulting as an initially exponential distribution that evolves into a power law scaling distribution.

Overall, the characterisation of fault strain distributions has provided insight on how the fault population evolves with time, the characteristics of which are not easily conveyed by conventional displacement-length plots. Given changes in scaling exponent are regarded as precursors to large earthquakes (Smith, 1981) and, for volcanic areas, precursors to eruptions (Gresta and Patane, 1983), we suggest that future work should provide a comprehensive, statistically robust investigation on fault scaling distributions that will enable a better understanding of fault evolution and its implication to related geohazard.

4.4. Off-fault deformation

Our results demonstrate that OFD accounts for at least 25 to 45% of total crustal strain, depending on the investigated rift parameters (Fig. 10). These results are consistent with the presence of so-called ‘hidden’ deformation, initially proposed by Kautz and Sclater (1988), where faults accommodated 40-50% of the known extension in clay analogue models, and 70-80% in sand analogue models. Our results lie within the range of 40% ± 23% OFD determined for the East Californian Shear Zone (Herbert et al., 2014) and within the range of OFD% calculated using ground-penetrating radar and palaeoseismic trench data, where drag folding and fault block rotations accommodated 46% of extension in the Taupo Rift (McClymont et al., 2010).

At the crustal scale, Marrett and Allmendinger (1992) and Walsh et al (1991) find that as much as 40% of the total extension is accounted for by small-scale faulting in seismically imaged extensional basins of the North Sea. In contrast, Scholz and Cowie (1990) argue that small-scale faulting accounted for less than 10% of the total strain budget, and Cowie (1995) reconcile both arguments by proposing that the relative importance of small faults decreases as the total strain increases due to strain localisation. As our results show that a significant proportion of strain is accommodated off-fault, such that deformation may be distributed in the form of fault drag, rotated fault blocks and/or pure bulk thinning of the crust, we suggest small-scale faulting (estimated through the extrapolation of fault size distributions) is not sufficient to account for total strain, and is only partially responsible for the discrepancy between summed fault strain and extension predicted by thermal subsidence (e.g. Marsden et al., 1990). In addition, our results show that OFD% progressively decreases to account for strain localisation, however we find that the decrease accounts for <10%, and overall OFD% may still remain relatively high by the end of model time (Fig. 10). This suggests that OFD% in the crust is inherent to fault evolution during continental extension.

Conclusions

1. We demonstrate that high-resolution 3D numerical models of continental extension statistically produce geologically realistic faulting patterns.
2. Numerical models show that fault patterns are rapidly established from the onset of extension (within <100 ka) and thus abide by the 'constant-length' fault growth model.
3. We find that distribution of initial strain and rate of fault weakening exert the strongest control on fault pattern variability- this highlights the significant role of pre-existing crustal fabric in controlling rift geometry
4. The scaling distribution of strain is not power law across all scales; instead all modelled fault populations are subject to an upper bound characteristic scale.
5. The amount of strain accommodated by faults is quantified, and we find that diffuse, off-fault deformation accounts for 25-45% of total crustal strain, the extent of which depends on rift parameters.
6. A robust statistical analysis of fault scaling distributions with consideration of sampling biases across scales is needed to fully deduce fault scaling laws.
7. The characterisation of strain distributions combined with a better understanding of OFD% may enable the future inversion of rift controls through observations alone.

Acknowledgements

PhD work is funded by Natural Environment Research Council (NERC) Centre for Doctoral Training (CDT) in Oil and Gas (NE/R01051X/1). The computational time for these simulations was provided under XSEDE project EAR180001. Alex Whittaker and Guillaume Duclaux are thanked for providing useful discussion during Sophie Pan's viva.

Open Research

The model simulations were run with ASPECT version 2.5.0-pre (main, e911bed). This specific version can be obtained by cloning the ASPECT repository (git clone https://github.com/geodynamics/aspect/) then within the repository checking out the specific commit (git checkout e911bed). ASPECT was compiled with deal.II 9.4.0, Trilinos 12.8.1, and p4est 2.3.2. dealII and the aforementioned libraries were compiled with the candi installation package (https:/github.com/dealii/candi, branch deal.II-9.4).

The ASPECT model data has been interpolated as 2D numpy files and are included in the supplementary files. From this, an image-processing based workflow is applied on the interpolated numpy files to automatically extract the faults – the python script is provided in the supplementary files. The script outputs a spreadsheet table with geometrical properties of each extracted fault, and a jupyter notebook in the supplementary file provides the code to reproduce the figures directly from the spreadsheet. The supplementary files can be found at https://figshare.com/s/dcc8ac81f0bd0fa50a0f.

References

Ackermann, R.V., Schlische, R.W. and Withjack, M.O., 2001. The geometric and statistical evolution of normal fault systems: an experimental study of the effects of mechanical layer thickness on scaling laws. Journal of Structural Geology, 23(11), pp.1803-1819.

Antonellini, M. and Aydin, A., 1994. Effect of faulting on fluid flow in porous sandstones: petrophysical properties. AAPG bulletin, 78(3), pp.355-377.

Argus, D.F. and Heflin, M.B., 1995. Plate motion and crustal deformation estimated with geodetic data from the Global Positioning System. Geophysical Research Letters, 22(15), pp.1973-1976.

Bailey, W.R., Walsh, J.J. and Manzocchi, T., 2005. Fault populations, strain distribution and basement fault reactivation in the East Pennines Coalfield, UK. Journal of Structural Geology, 27(5), pp.913-928.

Bell, R.E., McNeill, L.C., Henstock, T.J. and Bull, J.M., 2011. Comparing extension on multiple time and depth scales in the Corinth Rift, Central Greece. Geophysical Journal International, 186(2), pp.463-470.

Bonnet, E., Bour, O., Odling, N.E., Davy, P., Main, I., Cowie, P. and Berkowitz, B., 2001. Scaling of fracture systems in geological media. Reviews of geophysics, 39(3), pp.347-383.

Buck, W.R., 1991. Modes of continental lithospheric extension. Journal of Geophysical Research: Solid Earth, 96(B12), pp.20161-20178.

Buiter, S.J. and Torsvik, T.H., 2014. A review of Wilson Cycle plate margins: A role for mantle plumes in continental break-up along sutures?. Gondwana Research, 26(2), pp.627-653.

Burov, E. and Cloetingh, S.A.P.L., 1997. Erosion and rift dynamics: new thermomechanical aspects of post-rift evolution of extensional basins. Earth and Planetary Science Letters, 150(1-2), pp.7-26.

Cartwright, J.A., Trudgill, B.D. and Mansfield, C.S., 1995. Fault growth by segment linkage: an explanation for scatter in maximum displacement and trace length data from the Canyonlands Grabens of SE Utah. Journal of structural Geology, 17(9), pp.1319-1326.

Chapman, D. S. (1986). Thermal gradients in the continental crust (Vol. 24(1), pp. 63–70). Geological Society, London, Special Publications.

Cladouhos, T.T. and Marrett, R., 1996. Are fault growth and linkage models consistent with power-law distributions of fault lengths?. Journal of Structural Geology, 18(2-3), pp.281-293.

Clark, R.M. and Cox, S.J.D., 1996. A modern regression approach to determining fault displacement-length scaling relationships. Journal of Structural Geology, 18(2-3), pp.147-152.

Clauset, A., Shalizi, C.R. and Newman, M.E., 2009. Power-law distributions in empirical data. SIAM review, 51(4), pp.661-703.

Coolbaugh, M.F., Raines, G.L., Zehner, R.E., Shevenell, L. and Williams, C.F., 2006. Prediction and discovery of new geothermal resources in the Great Basin: Multiple evidence of a large undiscovered resource base. In GRC 2006 Annual Meeting: Geothermal Resources-Securing Our Energy Future (Vol. 30, pp. 867-873).

Corti, G., 2008. Control of rift obliquity on the evolution and segmentation of the main Ethiopian rift. Nature Geoscience, 1(4), pp.258-262.

Corti, G., Bonini, M., Innocenti, F., Manetti, P., Mulugeta, G., Sokoutis, D. and Cloetingh, S., 2003. Rift-parallel magma migration and localisation of magmatic activity in transfer zones. Acta Vulcanologica, 14(1/2), p.17.

Cowie, P.A., 1998. A healing–reloading feedback control on the growth rate of seismogenic faults. Journal of Structural Geology, 20(8), pp.1075-1087.

Cowie, P.A., Gupta, S. and Dawers, N.H., 2000. Implications of fault array evolution for synrift depocentre development: insights from a numerical fault growth model. Basin Research, 12(3-4), pp.241-261.

Cowie, P.A., Roberts, G.P., Bull, J.M. and Visini, F., 2012. Relationships between fault geometry, slip rate variability and earthquake recurrence in extensional settings. Geophysical Journal International, 189(1), pp.143-160.

Cowie, P.A., Sornette, D. and Vanneste, C., 1995. Multifractal scaling properties of a growing fault population. Geophysical Journal International, 122(2), pp.457-469.

Cowie, P.A., Vanneste, C. and Sornette, D., 1993. Statistical physics model for the spatiotemporal evolution of faults. Journal of Geophysical Research: Solid Earth, 98(B12), pp.21809-21821.

Daly, M.C., Andrade, V., Barousse, C.A., Costa, R., McDowell, K., Piggott, N. and Poole, A.J., 2014. Brasiliano crustal structure and the tectonic setting of the Parnaíba basin of NE Brazil: results of a deep seismic reflection profile. Tectonics, 33(11), pp.2102-2120.

Damsleth, E., Sangolt, V. and Aamodt, G., 1998, September. Sub-seismic faults can seriously affect fluid flow in the njord field off western norway-a stochastic fault modeling case study. In SPE Annual Technical Conference and Exhibition. OnePetro.

Davy, P., 1993. On the frequency-length distribution of the San Andreas fault system. Journal of Geophysical Research: Solid Earth, 98(B7), pp.12141-12151.

Dawers, N.H. and Anders, M.H., 1995. Displacement-length scaling and fault linkage. Journal of Structural Geology, 17(5), pp.607-614.

Dunbar, J.A. and Sawyer, D.S., 1989. How preexisting weaknesses control the style of continental breakup. Journal of Geophysical Research: Solid Earth, 94(B6), pp.7278-7292.

Ebinger, C.J., Jackson, J.A., Foster, A.N. and Hayward, N.J., 1999. Extensional basin geometry and the elastic lithosphere. Philosophical Transactions of the Royal Society of London. Series A: Mathematical, Physical and Engineering Sciences, 357(1753), pp.741-765.

Faulds, J. and Hinz, N., 2015, April. Favorable tectonic and structural settings of geothermal systems in the Great Basin region, western USA: Proxies for discovering blind geothermal systems. In Proceedings World Geothermal Congress, Melbourne, Australia, 19-25 April 2015 (No. DOE-UNR-06731-02). Nevada Bureau of Mines and Geology, University of Nevada, Reno.

Ferrill, D.A., Morris, A.P. and McGinnis, R.N., 2009. Crossing conjugate normal faults in field exposures and seismic data. AAPG bulletin, 93(11), pp.1471-1488.

Fletcher, R.C. and Hallet, B., 1983. Unstable extension of the lithosphere: A mechanical model for basin-and-range structure. Journal of Geophysical Research: Solid Earth, 88(B9), pp.7457-7466.

Gawthorpe, R.L., Jackson, C.A.L., Young, M.J., Sharp, I.R., Moustafa, A.R. and Leppard, C.W., 2003. Normal fault growth, displacement localisation and the evolution of normal fault populations: the Hammam Faraun fault block, Suez rift, Egypt. Journal of Structural Geology, 25(6), pp.883-895.

Gleason, G. C., & Tullis, J. (1995). A flow law for dislocation creep of quartz aggregates determined with the molten salt cell. Tectonophysics, 247(1), 1–23. https://doi.org/10.1016/0040-1951(95)00011-b

Glerum, A., Thieulot, C., Fraters, M., Blom, C., & Spakman, W. (2018). Nonlinear viscoplasticity in ASPECT: Benchmarking and applications to subduction. Solid Earth, 9(2), 267–294. https://doi.org/10.5194/se-9-267-2018

Gresta, S. and Patanè, G., 1983. Variation ofb values before the Etnean eruption of March 1981. pure and applied geophysics, 121(2), pp.287-295.

Gudmundsson, A., De Guidi, G. and Scudero, S., 2013. Length–displacement scaling and fault growth. Tectonophysics, 608, pp.1298-1309.

Gupta, A. and Scholz, C.H., 2000. A model of normal fault interaction based on observations and theory. Journal of structural Geology, 22(7), pp.865-879.

Gutenberg, B. and Richter, C.F., 1956. Earthquake magnitude, intensity, energy, and acceleration: (Second paper). Bulletin of the seismological society of America, 46(2), pp.105-145.

Heister, T., Dannberg, J., Gassmöller, R. and Bangerth, W., 2017. High accuracy mantle convection simulation through modern numerical methods–II: realistic models and problems. Geophysical Journal International, 210(2), pp.833-851.

Herbert, J.W., Cooke, M.L., Oskin, M. and Difo, O., 2014. How much can off-fault deformation contribute to the slip rate discrepancy within the eastern California shear zone?. Geology, 42(1), pp.71-75.

Hirth, G., & Kohlstedf, D. (2003). Rheology of the upper mantle and the mantle wedge: A view from the experimentalists (Vol. 138, pp. 83–106). Geophysical Monograph-American Geophysical Union. https://doi.org/10.1029/138gm06

Huismans, R.S. and Beaumont, C., 2003. Symmetric and asymmetric lithospheric extension: Relative effects of frictional-plastic and viscous strain softening. Journal of Geophysical Research: Solid Earth, 108(B10).

Jackson, C.A.L., Bell, R.E., Rotevatn, A. and Tvedt, A.B., 2017. Techniques to determine the kinematics of synsedimentary normal faults and implications for fault growth models. Geological Society, London, Special Publications, 439(1), pp.187-217.

Jackson, P. and Sanderson, D.J., 1992. Scaling of fault displacements from the Badajoz-Cordoba shear zone, SW Spain. Tectonophysics, 210(3-4), pp.179-190.

Kagan, Y.Y., 1999. Universality of the seismic moment-frequency relation. In Seismicity patterns, their statistical significance and physical meaning (pp. 537-573). Birkhäuser, Basel.

Kakimi, T., 1980. Magnitude-frequency relation for displacement of minor faults and its significnce in crustal deformation. Chishitsu Chosasho Geppo;(Japan), 31(10).

Kaldi, J., Daniel, R., Tenthorey, E., Michael, K., Schacht, U., Nicol, A., Underschultz, J. and Backe, G., 2013. Containment of CO2 in CCS: Role of Caprocks and Faults. Energy Procedia, 37, pp.5403-5410.

Kanamori, H. and Anderson, D.L., 1975. Theoretical basis of some empirical relations in seismology. Bulletin of the seismological society of America, 65(5), pp.1073-1095.

Kautz, S.A. and Sclater, J.G., 1988. Internal deformation in clay models of extension by block faulting. Tectonics, 7(4), pp.823-832.

Knott, S.D., Beach, A., Brockbank, P.J., Brown, J.L., McCallum, J.E. and Welbon, A.I., 1996. Spatial and mechanical controls on normal fault populations. Journal of Structural Geology, 18(2-3), pp.359-372.

Kooi, H., Cloetingh, S. and Burrus, J., 1992. Lithospheric necking and regional isostasy at extensional basins 1. Subsidence and gravity modeling with an application to the Gulf of Lions margin (SE France). Journal of Geophysical Research: Solid Earth, 97(B12), pp.17553-17571.

Kostrov, V.V., 1974. Seismic moment and energy of earthquakes, and seismic flow of rock. Izv. Acad. Sci. USSR Phys. Solid Earth, Engl. Transl., 1, pp.23-44.

Kronbichler, M., Heister, T. and Bangerth, W., 2012. High accuracy mantle convection simulation through modern numerical methods. Geophysical Journal International, 191(1), pp.12-29.

Main, I., 2000. Apparent breaks in scaling in the earthquake cumulative frequency-magnitude distribution: fact or artifact?. Bulletin of the Seismological Society of America, 90(1), pp.86-97.

Marrett, R. and Allmendinger, R.W., 1992. Amount of extension on" small" faults: An example from the Viking graben. Geology, 20(1), pp.47-50.

McClymont, A.F., Green, A.G., Kaiser, A., Horstmeyer, H. and Langridge, R., 2010. Shallow fault segmentation of the Alpine fault zone, New Zealand revealed from 2-and 3-D GPR surveying. Journal of Applied Geophysics, 70(4), pp.343-354.

Meyer, V., Nicol, A., Childs, C., Walsh, J.J. and Watterson, J., 2002. Progressive localisation of strain during the evolution of a normal fault population. Journal of Structural Geology, 24(8), pp.1215-1231.

Michas, G., Vallianatos, F. and Sammonds, P., 2015. Statistical mechanics and scaling of fault populations with increasing strain in the Corinth Rift. Earth and Planetary Science Letters, 431, pp.150-163.

Molnar, P. and Chen, W.P., 1983. Focal depths and fault plane solutions of earthquakes under the Tibetan plateau. Journal of Geophysical Research: Solid Earth, 88(B2), pp.1180-1196.

Morley, C.K., 1999. How successful are analogue models in addressing the influence of pre-existing fabrics on rift structure?. Journal of Structural Geology, 21(8-9), pp.1267-1274.

Naliboff, J.B., Glerum, A., Brune, S., Péron-Pinvidic, G. and Wrona, T., 2020. Development of 3-D rift heterogeneity through fault network evolution. Geophysical Research Letters, 47(13), p.e2019GL086611.

Odling, N.E., 1997. Scaling and connectivity of joint systems in sandstones from western Norway. Journal of Structural Geology, 19(10), pp.1257-1271.

Pan, S., Bell, R.E., Jackson, C.A.L. and Naliboff, J., 2022. Evolution of normal fault displacement and length as continental lithosphere stretches. Basin Research, 34(1), pp.121-140.

Pan, S., Naliboff, J., Bell, R., & Jackson, C. (2022). Bridging spatiotemporal scales of normal fault growth during continental extension using high-resolution 3D numerical models. Geochemistry, Geophysics, Geosystems, 23, e2021GC010316. https://doi.org/10.1029/2021GC010316

Peron-Pinvidic, G., Manatschal, G. and "IMAGinING RIFTING" Workshop Participants, 2019. Rifted margins: State of the art and future challenges. Frontiers in Earth Science, 7, p.218.

Phillips, T.B., Jackson, C.A., Bell, R.E., Duffy, O.B. and Fossen, H., 2016. Reactivation of intrabasement structures during rifting: A case study from offshore southern Norway. Journal of Structural Geology, 91, pp.54-73.

Pickering, G., Bull, J.M. and Sanderson, D.J., 1995. Sampling power-law distributions. Tectonophysics, 248(1-2), pp.1-20.

Rey, P.F., Teyssier, C. and Whitney, D.L., 2009. Extension rates, crustal melting, and core complex dynamics. Geology, 37(5), pp.391-394.

Rose, I., Buffett, B., & Heister, T. (2017). Stability and accuracy of free surface time integration in viscous flows. Physics of the Earth and Planetary Interiors, 262, 90–100.

Rotevatn, A., Jackson, C.A.L., Tvedt, A.B., Bell, R.E. and Blækkan, I., 2019. How do normal faults grow?. Journal of Structural Geology, 125, pp.174-184.

Rybacki, E., Gottschalk, M., Wirth, R., & Dresen, G. (2006). Influence of water fugacity and activation volume on the flow properties of fine-grained anorthite aggregates. Journal of Geophysical Research, 111(B3). https://doi.org/10.1029/2005jb003663

Scholz, C.H. and Contreras, J.C., 1998. Mechanics of continental rift architecture. Geology, 26(11), pp.967-970.

Scholz, C.H. and Cowie, P.A., 1990. Determination of total strain from faulting using slip measurements. Nature, 346(6287), pp.837-839.

Scholz, C.H., 1997. Size distributions for large and small earthquakes. Bulletin of the Seismological Society of America, 87(4), pp.1074-1077.

Scholz, C.H., Dawers, N.H., Yu, J.Z., Anders, M.H. and Cowie, P.A., 1993. Fault growth and fault scaling laws: Preliminary results. Journal of Geophysical Research: Solid Earth, 98(B12), pp.21951-21961.

Schultz, R.A. and Fossen, H., 2008. Terminology for structural discontinuities. AAPG bulletin, 92(7), pp.853-867.

Schultz, R.A., Soliva, R., Fossen, H., Okubo, C.H. and Reeves, D.M., 2008. Dependence of displacement–length scaling relations for fractures and deformation bands on the volumetric changes across them. Journal of Structural Geology, 30(11), pp.1405-1411.

Smith, W.D., 1981. The b-value as an earthquake precursor. Nature, 289(5794), pp.136-139.

Sorkhabi, R. and Tsuji, Y., 2005. The place of faults in petroleum traps.

Sornette, A. and Sornette, D., 1990. Earthquake rupture as a critical point: Consequences for telluric precursors. Tectonophysics, 179(3-4), pp.327-334.

Spyropoulos, C., Griffith, W.J., Scholz, C.H. and Shaw, B.E., 1999. Experimental evidence for different strain regimes of crack populations in a clay model. Geophysical Research Letters, 26(8), pp.1081-1084.

Tommasi, A. and Vauchez, A., 2001. Continental rifting parallel to ancient collisional belts: an effect of the mechanical anisotropy of the lithospheric mantle. Earth and Planetary Science Letters, 185(1-2), pp.199-210.

Torabi, A. and Berg, S.S., 2011. Scaling of fault attributes: A review. Marine and Petroleum Geology, 28(8), pp.1444-1460.

Turcotte, D.L., 2007. Self-organized complexity in geomorphology: Observations and models. Geomorphology, 91(3-4), pp.302-310.

Vallianatos, F., 2013. On the non-extensivity in Mars geological faults. EPL (Europhysics Letters), 102(2), p.28006.

Versfelt, J. and Rosendahl, B.R., 1989. Relationships between pre-rift structure and rift architecture in Lakes Tanganyika and Malawi, East Africa. Nature, 337(6205), pp.354-357.

Villemin, T., Angelier, J. and Sunwoo, C., 1995. Fractal distribution of fault length and offsets: Implications of brittle deformation evaluation—The Lorraine Coal Basin. In Fractals in the Earth Sciences (pp. 205-226). Springer, Boston, MA.

Walsh, J.J. and Watterson, J., 1991. Geometric and kinematic coherence and scale effects in normal fault systems. Geological Society, London, Special Publications, 56(1), pp.193-203.

Walsh, J.J., Childs, C., Imber, J., Manzocchi, T., Watterson, J. and Nell, P.A.R., 2003. Strain localisation and population changes during fault system growth within the Inner Moray Firth, Northern North Sea. Journal of Structural Geology, 25(2), pp.307-315.

Walsh, J.J., Nicol, A. and Childs, C., 2002. An alternative model for the growth of faults. Journal of Structural Geology, 24(11), pp.1669-1675.

Willemse, E.J., Pollard, D.D. and Aydin, A., 1996. Three-dimensional analyses of slip distributions on normal fault arrays with consequences for fault scaling. Journal of Structural Geology, 18(2-3), pp.295-309.

Wojtal, S., 1986. Deformation within foreland thrust sheets by populations of minor faults. Journal of Structural Geology, 8(3-4), pp.341-360.

Wojtal, S.F., 1994. Fault scaling laws and the temporal evolution of fault systems. Journal of Structural Geology, 16(4), pp.603-612.

Wojtal, S.F., 1996. Changes in fault displacement populations correlated to linkage between faults. Journal of Structural Geology, 18(2-3), pp.265-279.

Yielding, G., Needham, T. and Jones, H., 1996. Sampling of fault populations using sub-surface data: a review. Journal of Structural Geology, 18(2-3), pp.135-146.

Ziegler, P.A. and Cloetingh, S., 2004. Dynamic processes controlling evolution of rifted basins. Earth-Science Reviews, 64(1-2), pp.1-50.

List of Figures

Figure 6. Reference Model A evolution statistics, showing **(a)** the cumulative scaling distribution of strain per fault at 0.1, 1, 2, 3, 4 and 5 Myrs extension, and **(b)** the summation of fault accommodated strain, and the summation of total strain in the crust. Strain-time values at 0.1, 1, 2, 3, 4 and 5 Myrs extension are coloured corresponding to timesteps highlighted in Fig. 6a. The difference between the two plotted trendlines is equivalent to the off-fault deformation. Note that the first 30 datapoints in Fig. 6a are discarded for fitting, the distribution of which is shown by the dashed grey line.

Figure 7. Models investigating extension rates of (a) 1.25 mm/yr and (b) 5 mm/yr models, respectively. The upper panels show the active deformation field (log scale) at 4 Myrs. The bottom panels show the evolution of fault strain scaling distributions at 1, 2, 3, 4 and 5 Myrs. The first 30 points have been discarded m(marked in grey) for curve fitting. Scaling parameters are indicated in the legend.

Figure 8. Models investigating how rheological parameters effect fault patterns. The upper panel shows active deformation at 2.5 Myrs, and faults are coloured by their strain. The bottom panel shows the corresponding scaling distribution of strain. We compare the reference model **(a)** where initial blocks are 2.5 km blocks, the friction and cohesion angle weaken by 2x, and contrast between initial blocks is between 0.5 – 1.5. The subsequent models vary one parameter where block contrast is 0.5 – 0.6 thus faults weaken at a greater rate **(b),** the initial wavelength of faults is over 5 km **(c),** and the friction and cohesion angle weaken by 4x **(d).**

Figure 9. Comparison of strain between models and observations, as **(a)** Strain (geometric moment) scaling distribution at 1 Myrs; and **(b)** Total strain accumulation accommodated extracted faults vs time. Known observational geometric moment distributions are plotted for the Exmouth Plateau (Pan et al., 2022a) and the Timor Sea (Meyer et al., 2002). Total strain accumulation is summed either across transects in the Corinth Rift (Bell et al., 2011) or in 3D (Pan et al., 2022a). Due to limitations in data and kinematic constraints, a range marked from upper and lower estimates are shown.

Figure 10. Percentage of strain that is accommodated by off-fault (i.e., non-extracted) deformation. The difference between the summed crustal strain and summed fault strain is calculated for each timestep. See Supplementary Figure 1 for the off-fault deformation of the reference model C. Each point represents one timestep.

Figure 11. Schematic evolution of fault distribution and network evolution.

Fig 1. Examples of naturally observable extensional systems, illustrating the different structural styles of rift basins.

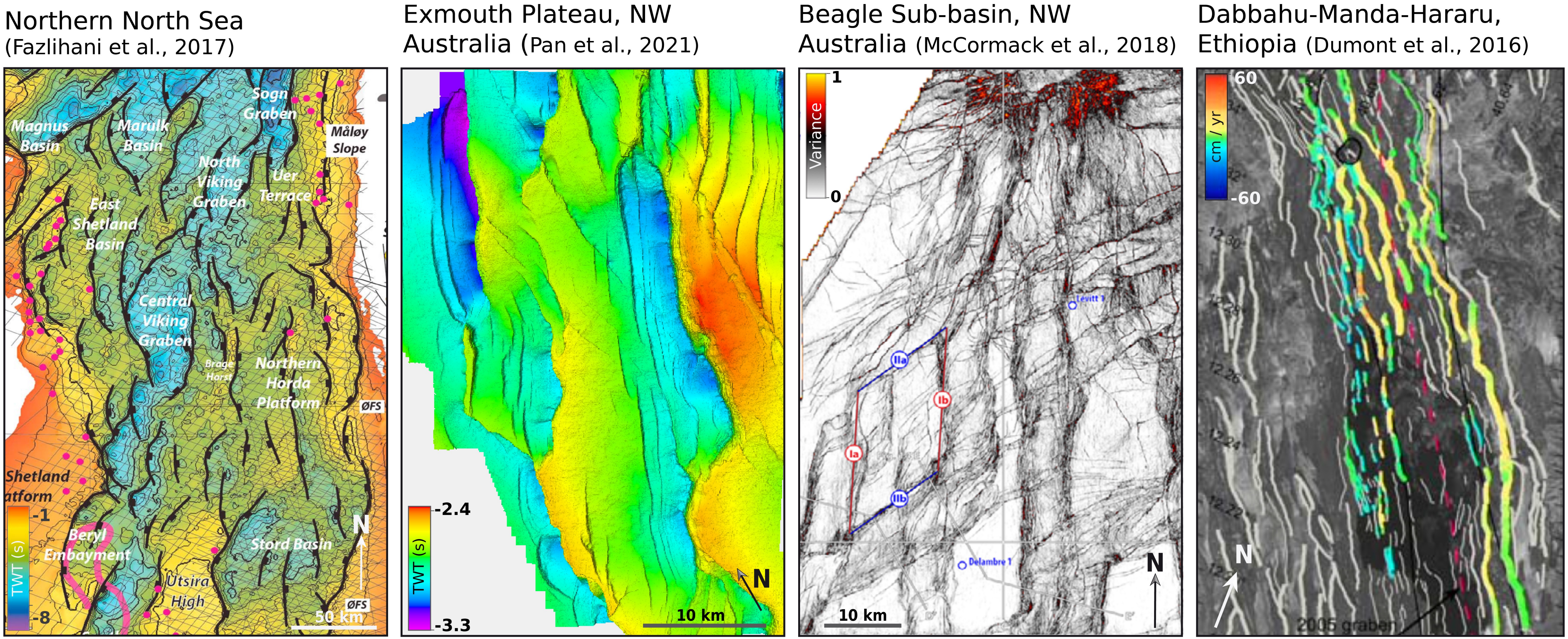

Fig 2. Cumulative frequency of a fault population distribution, fitted by power, gamma and exponential scaling laws. Points in dark grey may be interpreted as sampling biases such as truncation and censorship (see right), therefore only the central portion of the slope is typically fitted to a power law distribution.

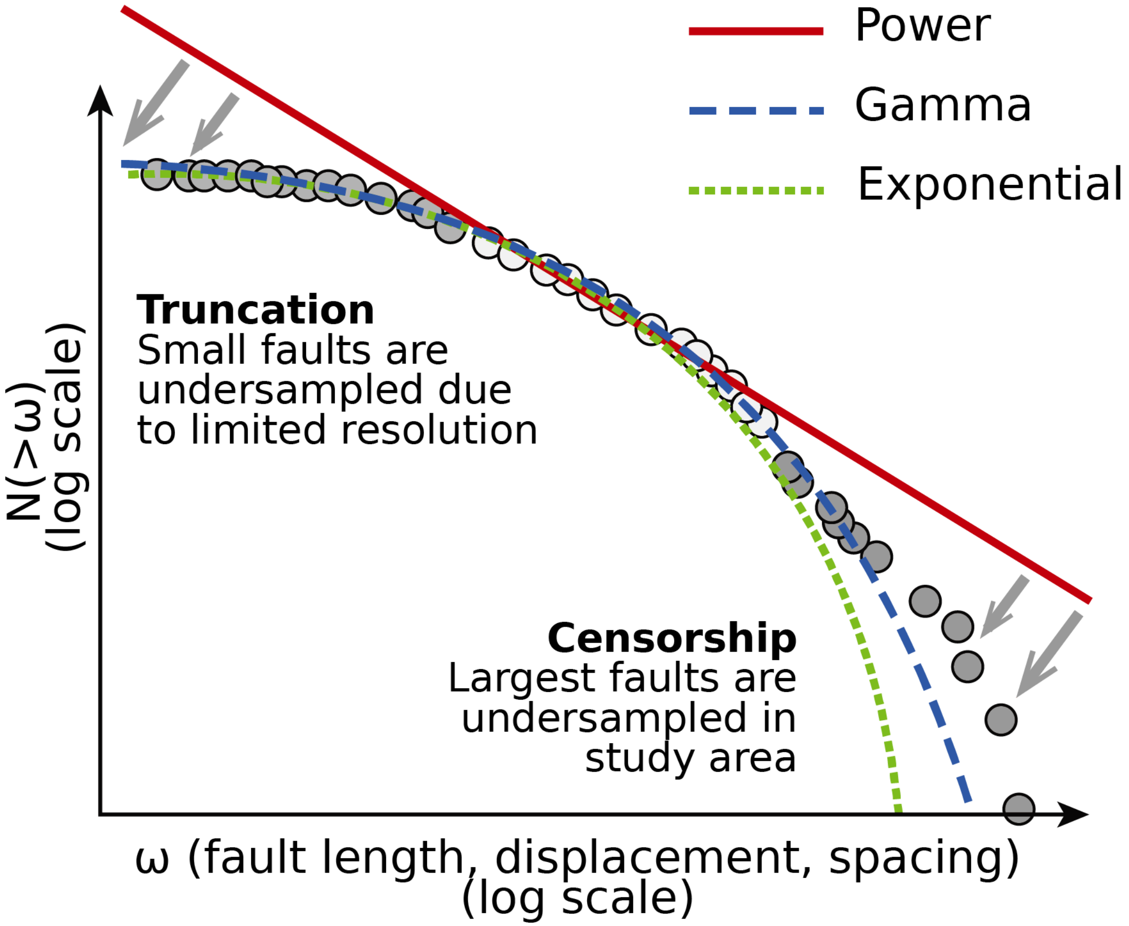

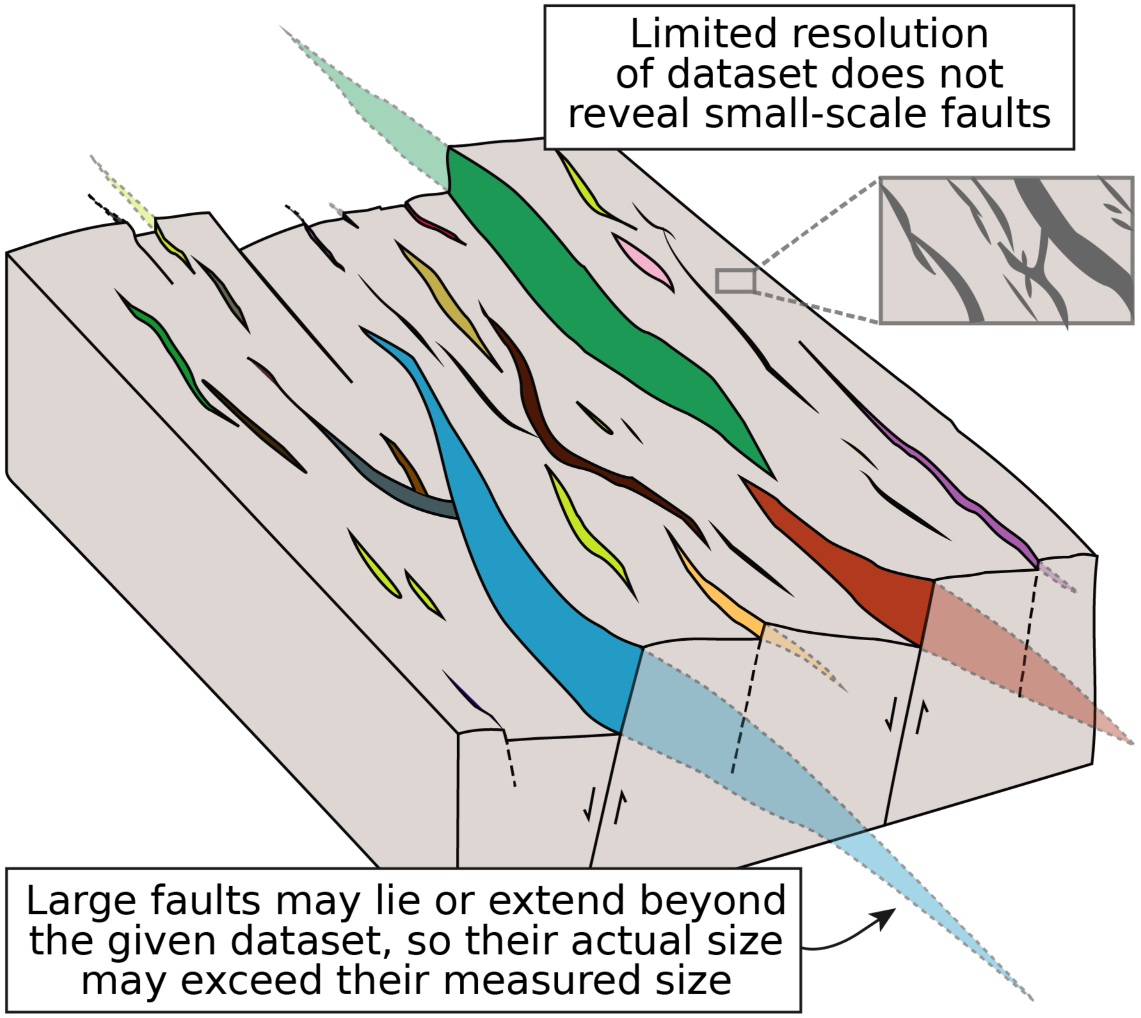

Fig 3. 5 models of continental extension, where Model A is the reference model, and we investigate the effects of a lower extension rate (B) and various rheology parameters in the model (C, D, E). For the models investigating rheology, their schematic weakening mechanisms are indicated on the right, and conceptual map view models of block distribution are indicated below. See Methods for full details.

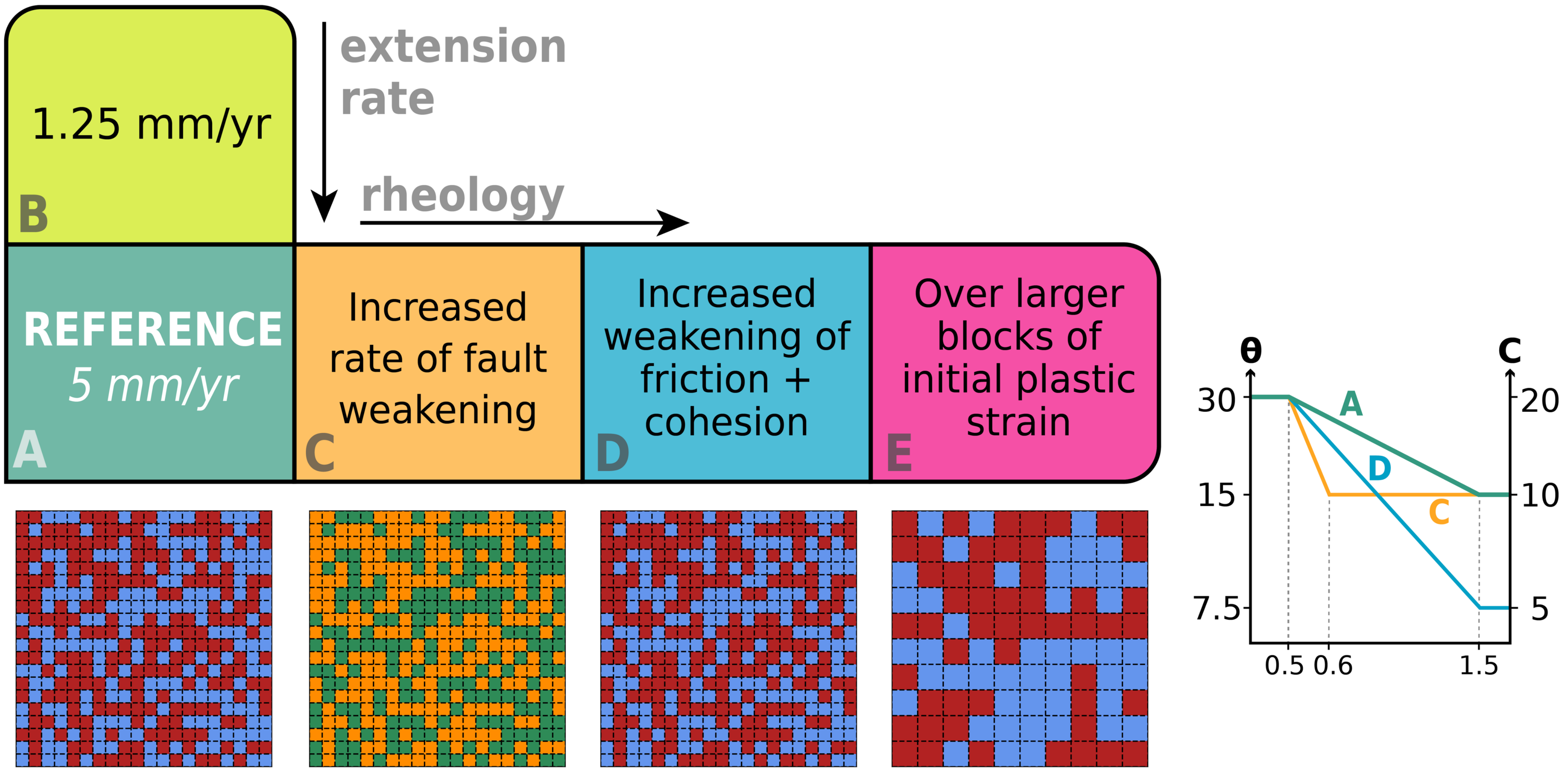

Fig 4. Active deformation (left) and accumulated brittle plastic deformation (right) at 5 Myrs rifting for Reference Model A (a and b) and Model H with increased fault weakening Model C (c and d).

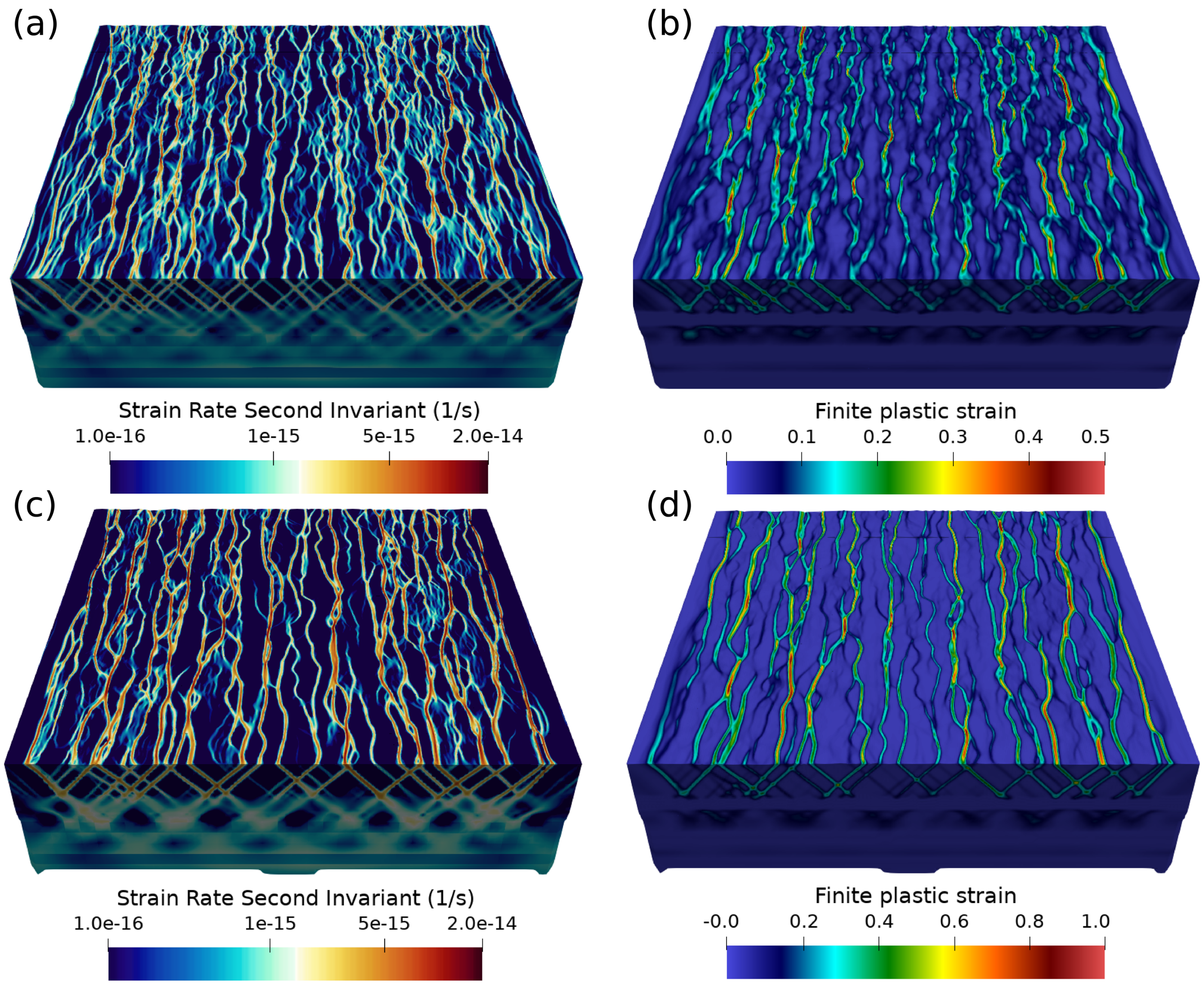

Fig 5. Strain extraction and summation (a) the plastic strain field, located 5 km beneath the initial model surface; (b) the strain rate second invariant; (c) discrete fault segments are extracted assigned a unique, accessible index; (d) labels masked over the cumulative plastic strain field equate to strain accommodated by faults; (e) fault lengths; (f) the geometric moment, which averages the plastic strain along their length

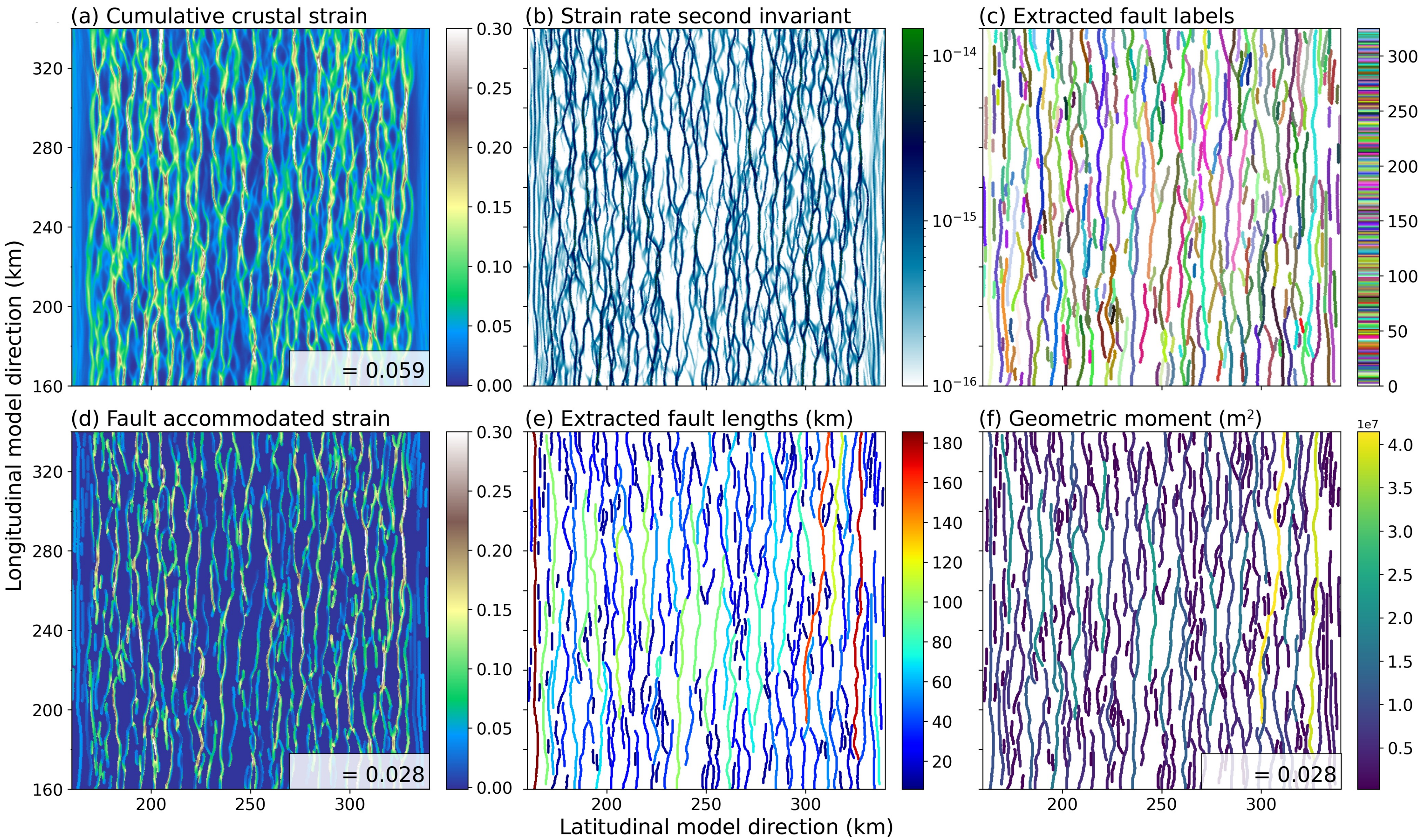

Fig 6. Reference Model A evolution statistics, showing **(a)** the cumulative scaling distribution of strain per fault at 0.1, 1, 2, 3, 4 and 5 Myrs extension, and **(b)** the summation of fault accommodated strain, and the summation of total strain in the crust. Strain-time values at 0.1, 1, 2, 3, 4 and 5 Myrs extension are coloured corresponding to timesteps highlighted in Fig. 6a. The difference between the two plotted trendlines is equivalent to the off-fault deformation. Note that the first 30 datapoints in Fig. 6a are discarded for fitting, the distribution of which is shown by the dashed grey line.

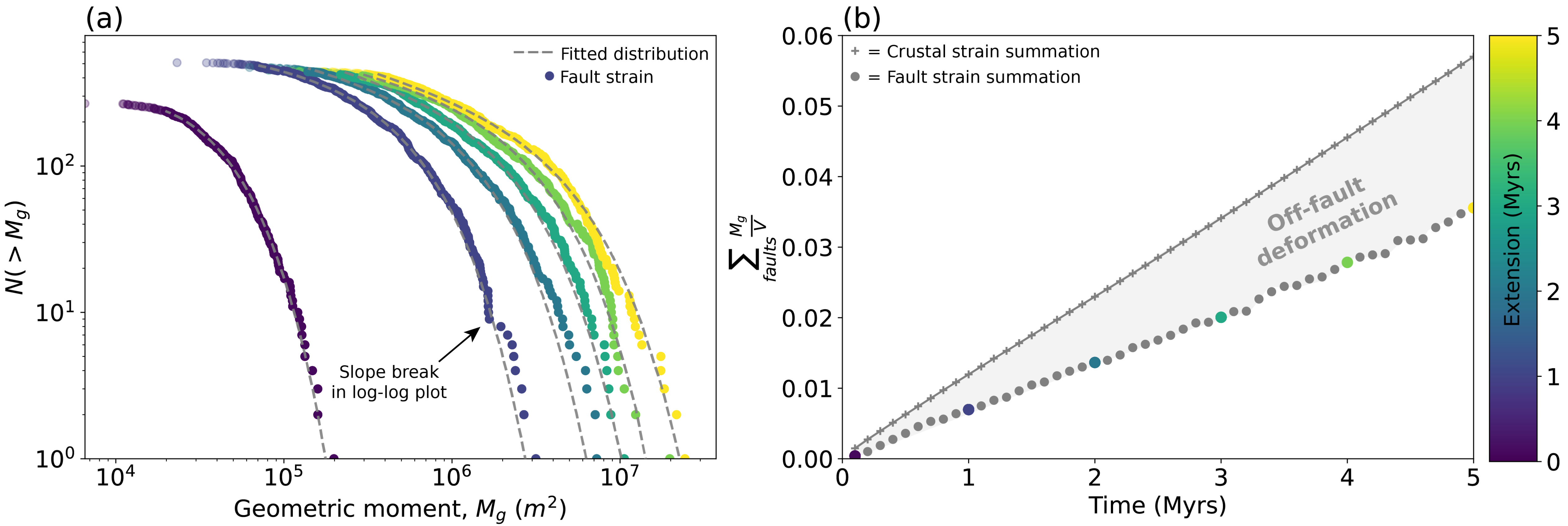

Fig 7. Models investigating extension rates of (a) 1.25 mm/yr and (b) 5 mm/yr models, respectively. The upper panels show the active deformation field (log scale) at 4 Myrs. The bottom panels show the evolution of fault strain scaling distributions at 1, 2, 3, 4 and 5 Myrs. The first 30 points have been discarded m(marked in grey) for curve fitting. Scaling parameters are indicated in the legend.

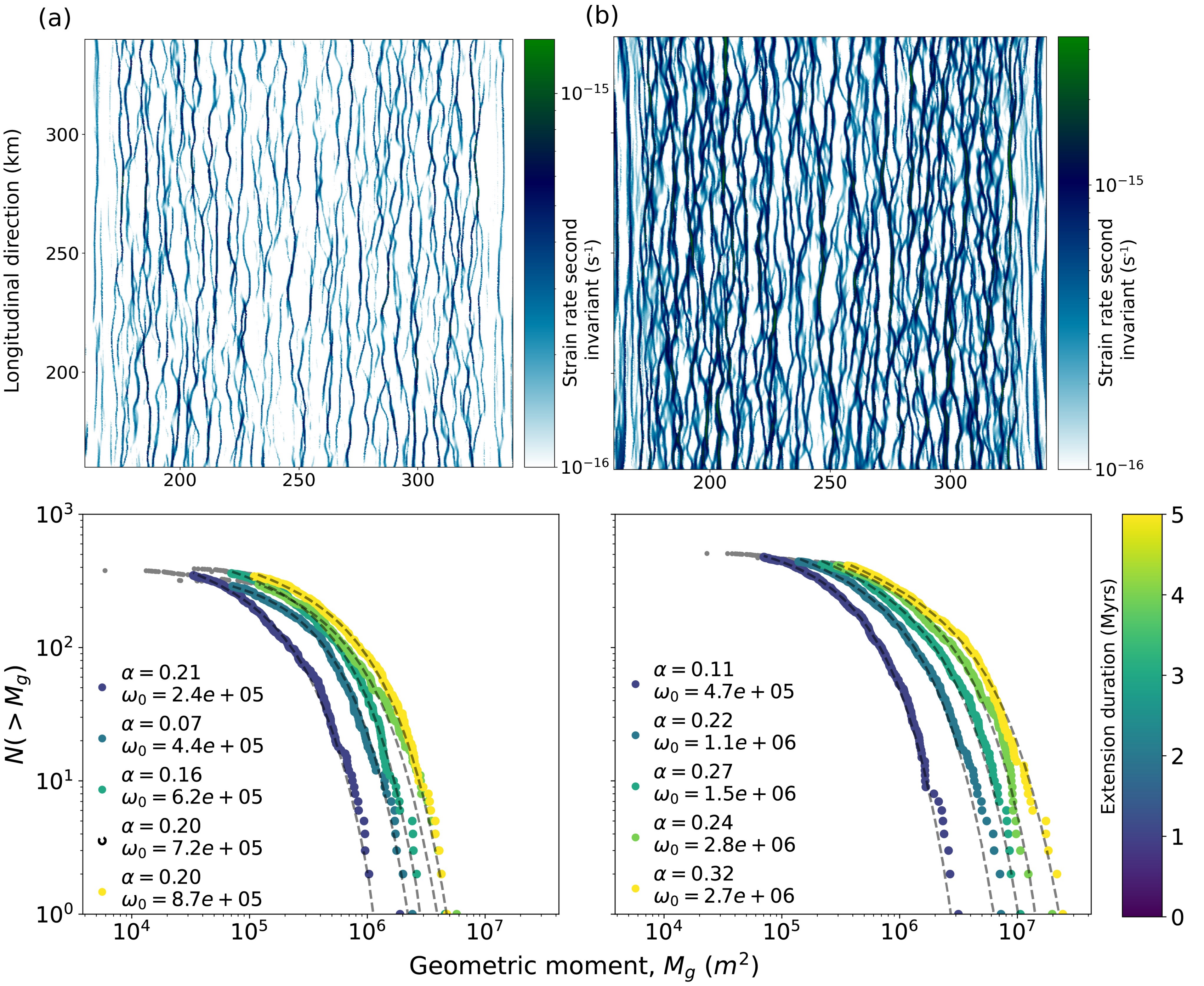

Fig 8. Models investigating how rheological parameters effect fault patterns. The upper panel shows active deformation at 2.5 Myrs, and faults are coloured by their strain. The bottom panel shows the corresponding scaling distribution of strain. We compare the reference model **(a)** where initial blocks are 2.5 km blocks, the friction and cohesion angle weaken by 2x, and contrast between initial blocks is between 0.5 – 1.5. The subsequent models vary one parameter where block contrast is 0.5 – 0.6 thus faults weaken at a greater rate **(b),** the initial wavelength of faults is over 5 km **(c),** and the friction and cohesion angle weaken by 4x **(d).**

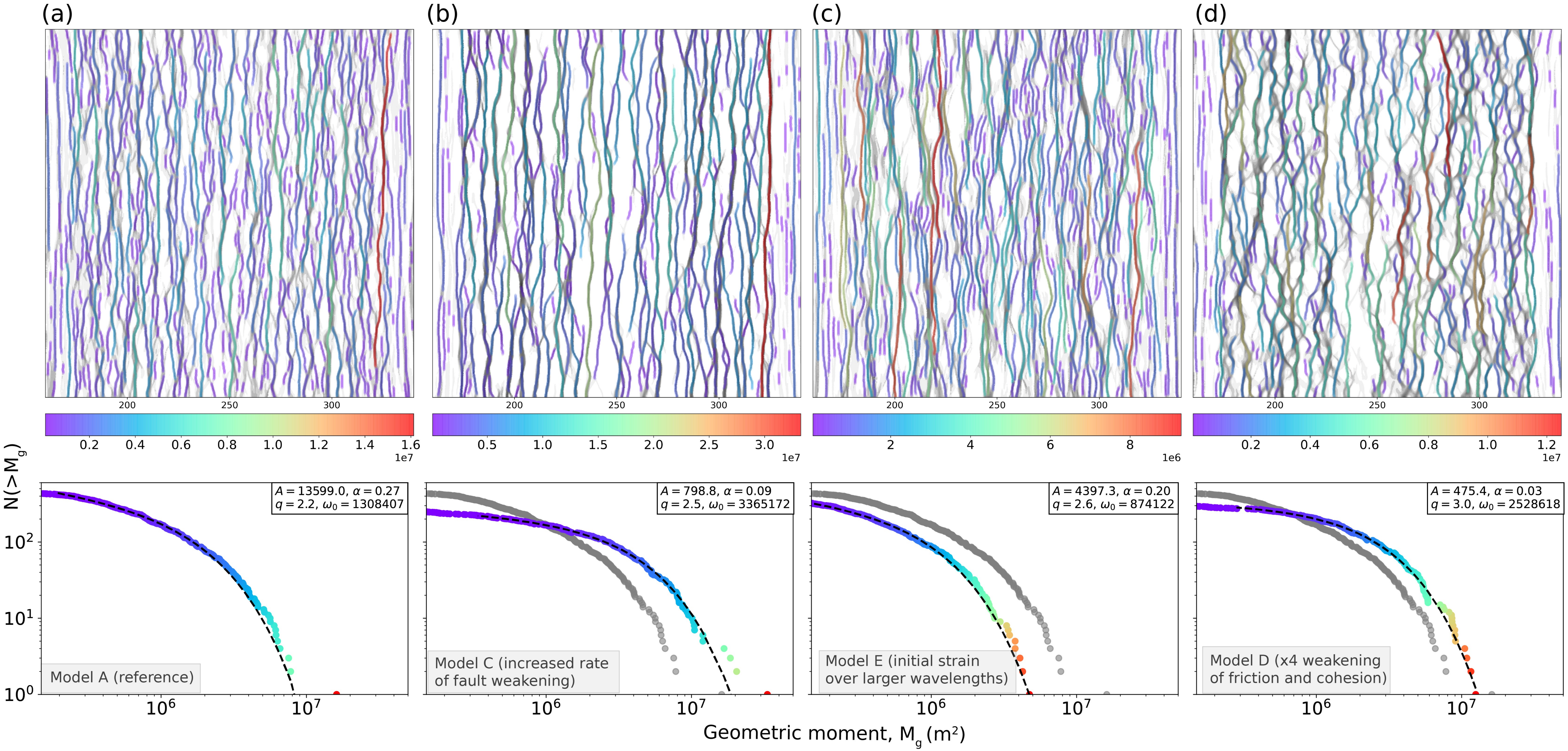

Fig 9. Comparison of strain between models and observations, as **(a)** Strain (geometric moment) scaling distribution at 1 Myrs; and **(b)** Total strain accumulation accommodated extracted faults vs time. Known observational geometric moment distributions are plotted for the Exmouth Plateau (Pan et al., 2022) and the Timor Sea (Meyer et al., 2002). Total strain accumulation is summed either across transects in the Corinth Rift (Bell et al., 2011) or in 3D (Pan et al., 2022). Due to limitations in data and kinematic constraints, a range marked from upper and lower estimates are shown.

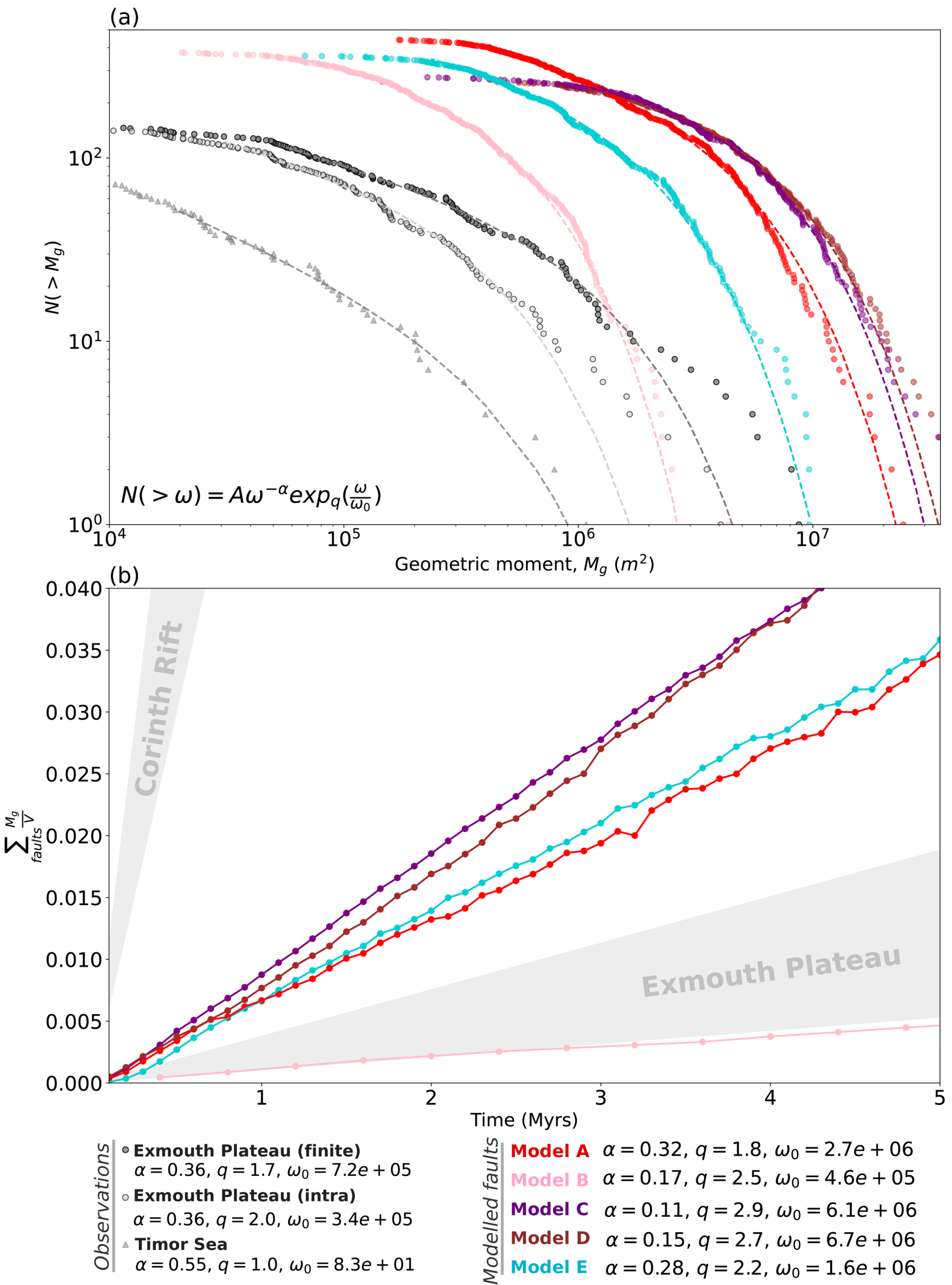

Fig 10. Percentage of strain that is accommodated by off-fault (i.e., non-extracted) deformation. The difference between the summed crustal strain and summed fault strain is calculated for each timestep. See Supplementary Figure 1 for the off-fault deformation of the reference model C. Each point represents one timestep.

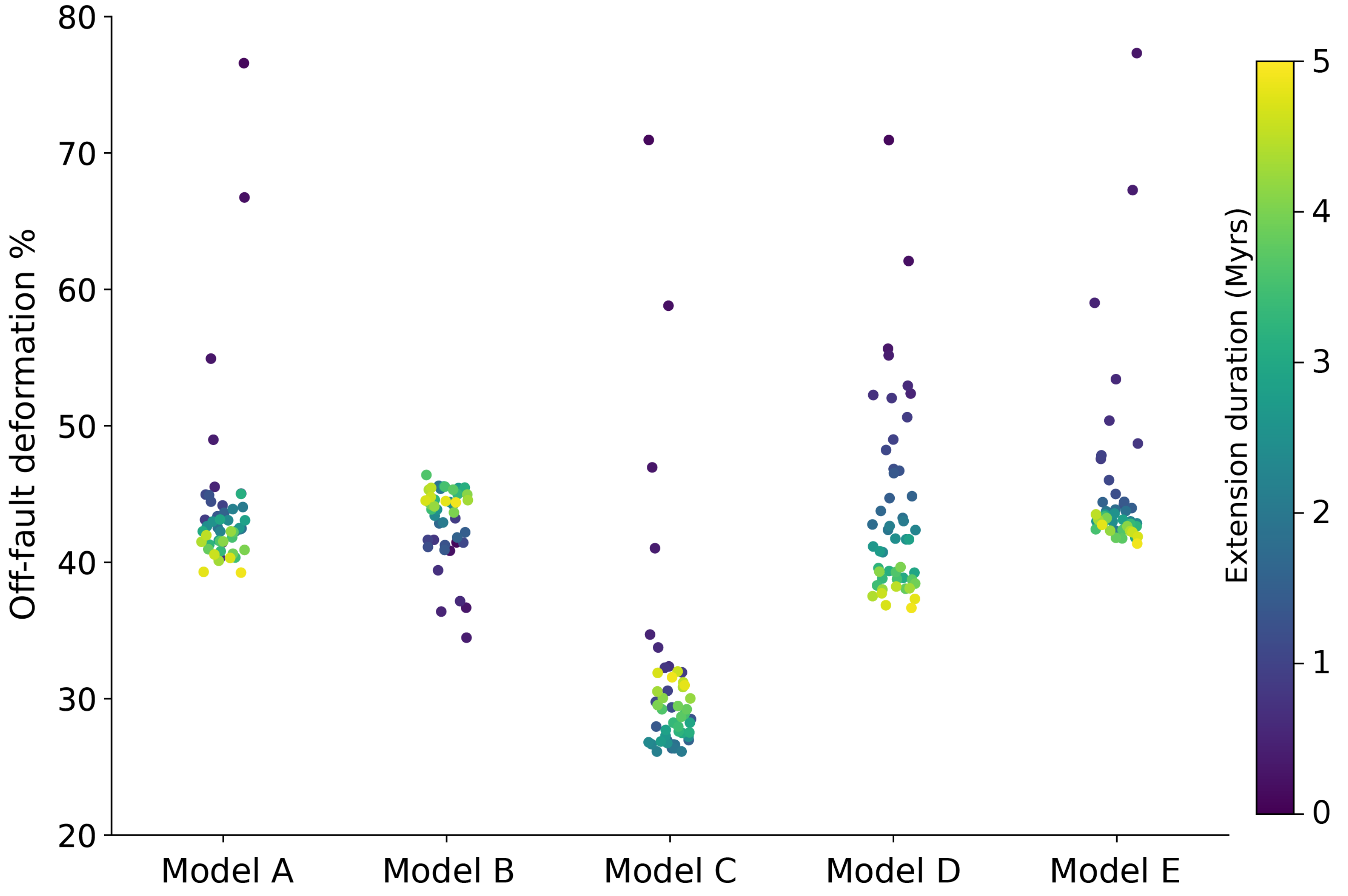

Fig 11. Schematic evolution of fault distribution and network evolution